Available online at www.sciencedirect.com
ScienceDirect
Mechanics Research Communications 35 (2008) 96–103
MECHANICS RESEARCH COMMUNICATIONS
www.elsevier.com/locate/mechrescom

Computation of compaction in compressible granular material

Michael T. Cochran [a,1], Joseph M. Powers [b,*]

[a] Core Furnace Systems Corporation, Coraopolis, PA 15108-3185, USA
[b] Department of Aerospace and Mechanical Engineering, University of Notre Dame, Notre Dame, IN 46556-5637, USA

Received 21 July 2007; received in revised form 28 September 2007
Available online 11 October 2007

Abstract

Equations modeling compaction in a mixture of granular high explosive and interstitial gas are solved numerically. Both phases are modeled as compressible, viscous fluids. This overcomes well known difficulties associated with computing shock jumps in the inviscid version of the equations, which cannot be posed in a fully conservative form. One-dimensional shock tube and piston-driven compaction solutions compare favorably with experiment and known analytic solutions. A simple two-dimensional extension is presented.

Keywords: Two-dimensional compaction; Granular flow; Continuum mixture theory

1. Introduction

It is well known that heterogeneous, porous, energetic, materials behave in dramatically different ways than do equivalent solid homogeneous energetic materials. In particular, porous media will show a greater tendency toward detonation with even modest stimuli (Gonthier and Powers, 2000). Of special importance is the compaction process, which is often the critical precursor to ignition and transition to detonation. As a precise understanding of the dynamics of such materials is important in a variety of aerospace and national defense applications, a large modeling literature has evolved (Gonthier and Powers, 2000; Baer and Nunziato, 1986; Baer, 1986; Powers et al., 1989, 1990; Bdzil et al., 1999; Kapila et al., 2001; Papalexandris, 2005; Lowe and Greenaway, 2005; Gonthier, 2004; Lowe and Longbottom, 2006). These models are focused on the continuum regime and do not consider individual grain behavior, which is typically at or below 10^{-4} m length scales. Nevertheless, the continuum model admits a broad variety of multiscale features, ranging from just above the grain scale to the device scale, which may be on the order of meters. In the literature, it is often unclear if the computational resolution necessary to capture all of the length scales inherent even for continuum models has been employed, as numerical diffusion associated with overly coarse grids smears the results in a way which may not be obvious.

* Corresponding author. Tel.: +1 574 631 5978; fax: +1 574 631 8341.
E-mail address: powers@nd.edu (J.M. Powers).
[1] Formely: University of Notre Dame, Notre Dame, IN 46556, USA.

0093-6413/$ - see front matter
doi:10.1016/j.mechrescom.2007.10.003

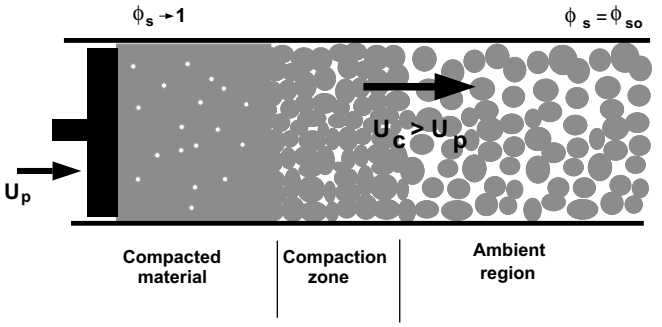

Fig. 1. Schematic of compaction phenomena induced by a piston.

Fig. 1 shows a schematic of a common benchmark experiment: compaction induced by a piston driving into the porous material (Sandusky and Bernecker, 1985; Sandusky and Liddiard, 1985). A propagating compaction wave leaves behind it a region that is almost completely solid. In contrast to most models of this experiment, which are formally inviscid and rely on numerical viscosity to capture grain-level phenomena, we employ the model of Powers (2004), who presents a simplified but useful model of physical diffusion which introduces a cut-off length scale at the grain level and models, in a rough sense, grain-scale interactions. This has the added advantage of rendering the model equations parabolic and, significantly, admits an unambiguously well-posed initial-boundary value problem; see also Vreman (2007). In contrast, many common inviscid models are hyperbolic, but lack a conservative form, so that shock jumps are impossible to determine analytically. Such models thus rely on a regularization via grid-dependent numerical viscosity to fix shock speeds, which themselves will have grid dependency. Moreover, it is often argued that this unusual regularization necessitates algorithmically exotic discretizations (Abgrall and Saurel, 2003) which in fact hinders widespread adaptation. A related situation in reactive gas dynamics is explored by Powers (2006), where it is shown that regularization via physical viscosity will suppress grid-dependent structures which commonly arise in inviscid simulations of two-dimensional detonations. Other common classes of inviscid, single pressure, two-phase models are well known to be formally ill-posed, which has induced a variety of complex remedies, (cf. Tiselj and Petelin, 1997).

Most relevant to the present study, Baer and Nunziato (1986) (BN) introduced an inviscid continuum theory for compaction. Baer (1986) and Powers et al. (1989) then examined steady compaction waves in such materials. Additional modeling issues were considered by Powers et al. (1990). In a series of papers by Bdzil et al. (1999) and Kapila et al. (2001), hereafter known as BMSKS, the model is further developed. Powers (2004) expanded the BMSKS model by explicitly including diffusion of momenta and energy. In addition to its well-posedness, it was shown that the model has full tensorial invariance, Galilean invariance, and satisfies an entropy inequality.

Nearly all of the research in this field has focused on one-dimensional limits of two-phase materials. This article contains a full two-dimensional analysis of the system presented by Powers (2004), and summarizes the work of Cochran (2007); it is the first to give explicit special care in resolving all two-dimensional flow structures. As shown by Powers (2004), the representative smallest continuum physical scales encountered in these problems are $\mathcal{O}(10^{-2}\ m)$. The grid resolution of the present calculations is $\Delta x \sim \mathcal{O}(10^{-3}\ \mathrm{m})$, thus capturing the small scale continuum physics. Problems with known solutions in the one-dimensional limit are solved, and then simple extensions into two dimensions are applied.

2. Model

2.1. Governing equations

The following evolution axioms are employed:

$$\frac{\partial}{\partial t}(\rho_s \phi_s) + \nabla \cdot (\rho_s \phi_s \mathbf{u}_s) = 0, \tag{1}$$

$$\frac{\partial}{\partial t}(\rho_g\phi_g) + \nabla\cdot(\rho_g\phi_g\mathbf{u_g}) = 0, \tag{2}$$

$$\frac{\partial}{\partial t}(\rho_s\phi_s\mathbf{u_s}) + \nabla\cdot(\rho_s\phi_s\mathbf{u_s}\mathbf{u_s}^T + \phi_s(p_s\mathbf{I} - \boldsymbol{\tau}_s)) = \mathscr{M}, \tag{3}$$

$$\frac{\partial}{\partial t}(\rho_g\phi_g\mathbf{u_g}) + \nabla\cdot\left(\rho_g\phi_g\mathbf{u_g}\mathbf{u_g}^T + \phi_g(p_g\mathbf{I} - \boldsymbol{\tau}_g)\right) = \mathscr{M}, \tag{4}$$

$$\frac{\partial}{\partial t}\left(\rho_s\phi_s\left(e_s + \frac{1}{2}\mathbf{u_s}\mathbf{u_s}^T\right)\right) + \nabla\cdot\left(\rho_s\phi_s\mathbf{u_s}\left(e_s + \frac{1}{2}\mathbf{u_s}\mathbf{u_s}^T\right) + \phi_s\mathbf{u_s}\cdot(p_s\mathbf{I} - \boldsymbol{\tau}_s) + \phi_s\mathbf{q_s}\right) = \mathscr{E}, \tag{5}$$

$$\frac{\partial}{\partial t}\left(\rho_g\phi_g\left(e_g + \frac{1}{2}\mathbf{u_g}\mathbf{u_g}^T\right)\right) + \nabla\cdot\left(\rho_g\phi_g\mathbf{u_g}\left(e_g + \frac{1}{2}\mathbf{u_g}\mathbf{u_g}^T\right) + \phi_s\mathbf{u_g}.(p_g\mathbf{I} - \boldsymbol{\tau}_g) + \phi_g\mathbf{q_g}\right) = -\mathscr{E}, \tag{6}$$

$$\frac{\partial}{\partial t}(\rho_s) + \nabla\cdot(\rho_s\mathbf{u_s}) = -\frac{\rho_s\mathscr{F}}{\phi_s}. \tag{7}$$

Eqs. (1)–(6) describe the evolution of mass, linear momenta, and energy; Eq. (7) accounts for compaction (Baer and Nunziato, 1986). Scalar quantities in Eqs. (1)–(7) are ρ, ϕ, p, e and T which represent intrinsic density, volume fraction, pressure, energy, and temperature, respectively. The subscripts s and g denote properties of the solid phase and the gas phase, respectively. The vector quantities $\mathbf{u}$ and $\mathbf{q}$ represent the velocity and the heat fluxes, while $\boldsymbol{\tau}$ is the viscous stress tensor for each phase. The terms $\mathscr{M}$ and $\mathscr{E}$ represent interphase transfer of momentum and energy between the gas and solid phases. The term $\mathscr{F}$ represents a source term for material compaction. Eqs. (1)–(6) are constructed to formally conserve mixture mass, momentum and energy. The forms chosen for $\mathscr{M}, \mathscr{E}$ and $\mathscr{F}$ are those given by BMSKS, taking the limit of negligible interphase drag and heat transfer.

$$\mathscr{M} = p_g\nabla\phi_s, \quad \mathscr{E} = -p_g\mathscr{F} + \mathbf{u}_s\cdot\mathscr{M}, \quad \mathscr{F} = \frac{\phi_s\phi_g}{\mu_c}(p_s - \beta_s - p_g). \tag{8}$$

This limit is justified in Powers (2004), where one finds that $\mathscr{F}$ is the main source of irreversibility. Here μ_c is the compaction viscocity; the configuration stress is β_s.

2.2. Constitutive relations

Closure of the system requires specifying constitutive equations:

$$p_s = \rho_s^2\frac{\partial\psi_s}{\partial\rho_s}|_{T_s\phi_s}, \quad p_g = \rho_g^2\frac{\partial\psi_s}{\partial\rho_g}|_{T_g}, \tag{9}$$

$$\eta_s = -\frac{\partial\psi_s}{\partial T_s}|_{\rho_s\phi_s}, \quad \eta_g = -\frac{\partial\psi_g}{\partial T_g}|_{\rho_g}, \tag{10}$$

$$e_s = \psi_s + T_s\eta_s, \quad e_g = \psi_g + T_g\eta_g, \tag{11}$$

$$\tau_s = 2\mu_s\left(\frac{(\nabla\mathbf{u}_s)^T + \nabla\mathbf{u}_s}{2} - \frac{1}{3}(\nabla\cdot\mathbf{u}_s)\mathbf{I}\right), \quad \tau_g = 2\mu_g\left(\frac{(\nabla\mathbf{u}_g)^T + \nabla\mathbf{u}_g}{2} - \frac{1}{3}(\nabla\cdot\mathbf{u}_g)\mathbf{I}\right), \tag{12}$$

$$\mathbf{q}_s = -k_s\nabla T_s, \quad \mathbf{q}_g = -k_g\nabla T_g, \tag{13}$$

$$\psi_s = \hat{\psi}(\rho_s, T_s) + B(\phi_s), \quad \psi_g = \psi_g(\rho_g, T_g), \tag{14}$$

$$\beta_s = \rho_s\phi_s\frac{\partial\psi_s}{\partial\phi_s}\bigg|_{\rho_s,T_s}, \tag{15}$$

$$\phi_s = 1 - \phi_g. \tag{16}$$

The following new parameters appear in Eqs. (9)–(16): coefficient of viscosity, μ and the coefficient of thermal conductivity, k. Helmholtz free energy, ψ, and entropy η are variables introduced into the system. Eqs. (9)–(11) are definitions of canonical thermodynamic relationships for pressure, energy and entropy. Eq. (12) gives statements of the standard Newtonian relations between viscous stresses and strain rate for isotropic

compressible fluids which satisfy Stokes' assumption. Eq. (13) states Fourier's law of heat transfer. Eq. (14) gives classical (as yet unspecified) equations of state for the solid and gas. The free energy associated with configurational stresses appears as the new variable $B(\phi)$. Eq. (15) gives the configurational stress, and Eq. (16) gives the saturation condition.

A standard virial equation of state for the gas is adopted (Powers, 2004) which yields expressions for gas pressure and energy:

$$\psi_{\mathrm{g}}(\rho_{\mathrm{g}}, T_{\mathrm{g}}) = c_{v\mathrm{g}} T_{\mathrm{g}} \left(1 - \ln\left(\frac{T_{\mathrm{g}}}{T_{\mathrm{g0}}}\right) + (\gamma_{\mathrm{g}} - 1)\left(\ln\left(\frac{\rho_{\mathrm{g}}}{\rho_{\mathrm{g0}}}\right) + b_{\mathrm{g}}(\rho_{\mathrm{g}} - \rho_{\mathrm{g0}}) \right) \right), \tag{17}$$

$$p_{\mathrm{g}} = (\gamma_{\mathrm{g}} - 1) c_{v\mathrm{g}} \rho_{\mathrm{g}} T_{\mathrm{g}} (1 + b_{\mathrm{g}} \rho_{\mathrm{g}}), \tag{18}$$

$$e_{\mathrm{g}} = c_{v\mathrm{g}} T_{\mathrm{g}}. \tag{19}$$

Here $c_{v\mathrm{g}}$ is the constant specific heat at constant volume for the gas; b_{g} is the virial coefficient; γ_{g} is the ratio of specific heats for the gas; and ρ_{g0} and T_{g0} are the initial, reference, states for the system.

Schewendeman et al. (2006) provides the specific form for ψ_{s} giving solid pressure, energy and configurational stress:

$$\begin{aligned} \psi_{\mathrm{s}}(\rho_{\mathrm{s}}, T_{\mathrm{s}}, \phi_{\mathrm{s}}) = {} & c_{v\mathrm{s}} T_{\mathrm{s}} \left(1 - \ln\left(\frac{T_{\mathrm{s}}}{T_{\mathrm{s0}}}\right) + (\gamma_{\mathrm{s}} - 1) \ln\left(\frac{\rho_{\mathrm{s}}}{\rho_{\mathrm{s0}}}\right) \right) + \frac{\epsilon_{\mathrm{s}} \rho_{\mathrm{s0}}}{\gamma_{\mathrm{s}} \rho_{\mathrm{s}}} \\ & + \frac{(p_{\mathrm{s0}} - p_{\mathrm{g0}})(2 - \phi_{\mathrm{s0}})^2}{\rho_{\mathrm{s0}} \phi_{\mathrm{s0}} \ln\left(\frac{1}{1-\phi_{\mathrm{s0}}}\right)} \ln\left(\left(\frac{2 - \phi_{\mathrm{s0}}}{2 - \phi_{\mathrm{s}}}\right) \frac{(1 - \phi_{\mathrm{s}})^{\frac{1-\phi_{\mathrm{s}}}{2-\phi_{\mathrm{s}}}}}{(1 - \phi_{\mathrm{s0}})^{\frac{1-\phi_{\mathrm{s0}}}{2-\phi_{\mathrm{s0}}}}} \right), \end{aligned} \tag{20}$$

$$p_{\mathrm{s}} = (\gamma_{\mathrm{s}} - 1) c_{v\mathrm{s}} \rho_{\mathrm{s}} T_{\mathrm{s}} - \frac{1}{\gamma_{\mathrm{s}}} \rho_{\mathrm{s0}} \epsilon_{\mathrm{s}}, \tag{21}$$

$$e_{\mathrm{s}} = c_{v\mathrm{s}} T_{\mathrm{s}} + \frac{\epsilon_{\mathrm{s}} \rho_{\mathrm{s0}}}{\gamma_{\mathrm{s}} \rho_{\mathrm{s}}} + \frac{(p_{\mathrm{s0}} - p_{\mathrm{g0}})(2 - \phi_{\mathrm{s0}})^2}{\rho_{\mathrm{s0}} \phi_{\mathrm{s0}} \ln\left(\frac{1}{1-\phi_{\mathrm{s0}}}\right)} \ln\left(\left(\frac{2 - \phi_{\mathrm{s0}}}{2 - \phi_{\mathrm{s}}}\right) \frac{(1 - \phi_{\mathrm{s}})^{\frac{1-\phi_{\mathrm{s}}}{2-\phi_{\mathrm{s}}}}}{(1 - \phi_{\mathrm{s0}})^{\frac{1-\phi_{\mathrm{s0}}}{2-\phi_{\mathrm{s0}}}}} \right), \tag{22}$$

$$\beta_{\mathrm{s}} = (p_{\mathrm{s0}} - p_{\mathrm{g0}}) \frac{\rho_{\mathrm{s}} \phi_{\mathrm{s}}}{\rho_{\mathrm{s0}} \phi_{\mathrm{s0}}} \left(\frac{2 - \phi_{\mathrm{s0}}}{2 - \phi_{\mathrm{s}}}\right)^2 \frac{\ln\left(\frac{1}{1-\phi_{\mathrm{s}}}\right)}{\ln\left(\frac{1}{1-\phi_{\mathrm{s0}}}\right)}. \tag{23}$$

As with the gas, $c_{v\mathrm{g}}$ and γ_{s} represent the constant of specific heat at constant volume, and the ratio of specific heats of the solid. The constants ρ_{s0}, T_{s0}, ϕ_{s0}, p_{s0} and p_{g0} are the initial states of solid density, solid temperature, solid volume fraction, solid pressure and gas pressure, respectively. The remaining parameters are ϵ_{s}, which is a factor used to match experimental data. Table 1 reports the values for all of the parameters in this paper.

Table 1
Parameter values used in this study

Parameter	Units	Value	Parameter	Units	Value
μ_{g}	Ns/m^2	1.0×10^{0}	ρ_{g0}	kg/m^3	1.0×10^{0}
μ_{s}	Ns/m^2	1.0×10^{3}	ρ_{s0}	kg/m^3	1.9×10^{3}
k_{g}	W/m/K	1.0×10^{3}	ϕ_{s0}		7.3×10^{-1}
k_{s}	W/m/K	1.0×10^{0}	T_{g0}	K	3.0×10^{2}
γ_{g}		2.7×10^{0}	T_{s0}	K	3.0×10^{2}
γ_{s}		5.0×10^{0}	$\hat{\rho}_{\mathrm{g}}$	kg/m^3	1.1×10^{0}
$c_{v\mathrm{g}}$	J/kg/K	2.4×10^{3}	$\hat{\rho}_{\mathrm{s}}$	kg/m^3	2.0×10^{0}
$c_{v\mathrm{s}}$	J/kg/K	1.5×10^{3}	ϵ_{s}	J/kg^3	8.98×10^{6}
μ_{c}	Ns/m^2	1.0×10^{3}	b_{g}	m^3/kg	1.1×10^{-3}
t_{rise}	s	1.0×10^{-6}	$u_{\mathrm{p}}^{\mathrm{max}}$	m/s	1.0×10^{2}

2.3. Boundary conditions

We consider only one-dimensional geometries with $x \in [0, L]$, and rectangular geometries in two dimensions, with $x \in [0, L]$, $y \in [0, H]$. For one-dimensional problems we take as boundary conditions $\partial T/\partial x = 0$ at $x = 0$ and $x = L$ and $u_s(0) = u_s(L) = u_g(0) = u_g(L) = 0$.

The two-dimensional problems have thermally insulated boundaries, $\nabla T_s = \nabla T_g = 0$, and satisfy no-slip boundary conditions:

$$u_s(y = 0, t) = u_s(y = H, t) = 0, \quad u_g(y = 0, t) = u_g(y = H, t) = 0, \tag{24}$$

$$v_s(y = 0, t) = v_s(x = L, t) = 0, \quad v_g(x = 0, t) = v_g(y = L, t) = 0. \tag{25}$$

2.4. Numerical method

The numerical algorithm embodied in the commercial software package FEMLAB (COMSOL, 2003) was used to solve the Eqs. (1)–(23). FEMLAB uses the method of lines to solve the problem. The spatial domain is first discretized into a number of finite elements, reducing the problem to a large system of ordinary differential equations (ODE's). The time advancement algorithm is a version of the differential/algebraic equation (DAE) solver, DASPK. This solver uses variable-order, variable-step-size backward differentiation formulas to generate a linear system at each time step. The resulting linear system is of the form $\mathbf{A} \cdot \mathbf{x} = \mathbf{b}$, and is solved via an LU factorization algorithm.

3. One-dimensional verification and validation problems

Two one-dimensional problems are were solved in Cochran (2007): a shock tube, which has an ideal-gas-limit analytic solution, used for verification, and a piston problem, for which good experimental data exists for validation. In order to estimate the convergence of the solver, an approximation of the local error

$$e_l = \frac{|\rho^e_{s\,\max} - \rho_{s\,\max}|}{\rho^e_{s\,\max}} \tag{26}$$

was used. Here $\rho_{s\,\max}$ is the maximum value of the solid density for the solution to the equation set for a given mesh and $\rho^e_{s\,\max}$ is the maximum value of the solid density for the solution to a highly resolved mesh, numbering 32,768 nodes, which is taken to be the exact solution to the problem. The estimate for Δx is the average distance between the nodes in the domain. The error e_l converges at a uniform rate of $\mathcal{O}(\Delta x^{2.7})$. It was necessary to do a simple point convergence test on these meshes, since the exact location of the node points shifted with each change in the mesh. A domain convergence test would be a better approximation of the error, and would give a better estimate of the convergence of the system.

A shock tube with two ideal, calorically perfect gases and $\mathscr{F} = 0$ was studied and is detailed in Cochran (2007). The region $x \in [0\text{ m}, 0.25\text{ m}]$ had increased densities, $\hat{\rho}_s$ and $\hat{\rho}_g$ (Table 1), for the solid and gas, respectively; the whole system started at rest, and at a uniform temperature. The results match remarkably well with the analytic solution. The only difference is that the predicted results have finite wave thicknesses in the shock and rarefaction zones due to physical diffusion.

For validation, a piston problem with $\mathscr{F} \neq 0$ and non-ideal state equations is considered; the system begins at rest, with uniform temperature profile. To model the piston problem, the reference frame is attached to the accelerating piston face, and the domain is subjected to a non-Galilean transformation (Cochran, 2007):

$$\hat{x} = x - u_p^{\max}\left(t + t_{\text{rise}}\left(\exp\left(-\frac{t}{t_{\text{rise}}}\right) - 1\right)\right); \quad \hat{t} = t. \tag{27}$$

Here, $u_p^{\max}$ is the maximum piston velocity, and t_{rise} is the rise time.

The result is that there is an effective body force introduced into Eqs. (3) and (4). Solving the piston problem results in a steady compaction wave in the long time limit, after a brief transient of similar duration as the very small $t_{\text{rise}} = 10^{-6}$ s. For example when $u_p^{\max} = 100$ m/s, there is a compaction wave traveling ahead of the

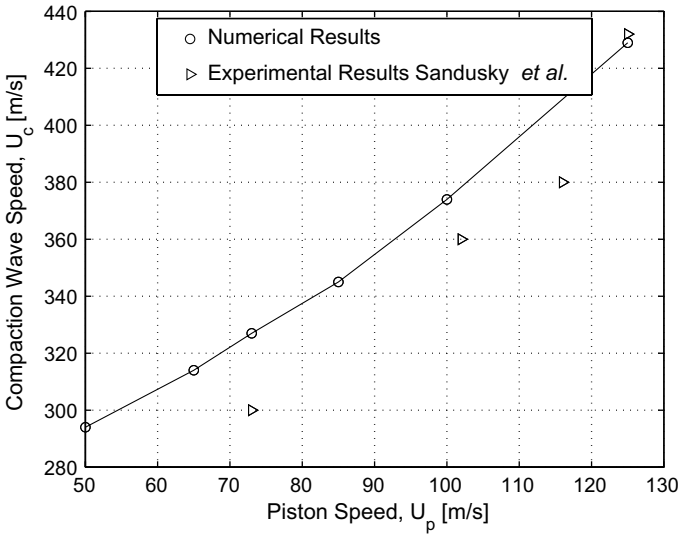

Fig. 2. Compaction wave speed versus piston speed showing both numerical and experimental results (Sandusky and Liddiard, 1985).

piston at a predicted speed of approximately 375 m/s. Experimental data show a compaction wave traveling at 360 m/s ahead of the 102 m/s piston. The discrepancy is likely due to the difficulty of determining the precise location of a wave front of finite thickness.

Fig. 2 shows the variation of the compaction wave speed, U_c for a range of piston speeds U_p. The experimental data from Sandusky and Liddiard (1985) is also shown. For many of the piston speeds, the predicted wave speeds are slightly higher, although the scatter of the data indicates that the numerical results are still in good agreement with the experimental results.

4. Two-dimensional problems

Next, the algorithm is shown to be valid for two-dimensional scenarios. Results here are confined to small deviations from the one-dimensional limit. We consider problems with $L = 0.5$ m, $H = 0.05$ m, noting that H is approaching, but not yet at the physical cutoff length scale of 0.01 m. Larger domains can and should be considered, at the expense of more computational resources.

4.1. Shock tube

The two-dimensional shock tube problem solved here is for a long narrow tube in the ideal gas limit with $\mathscr{F} = 0$. A cross section of the domain, Fig. 3, through the center of the shock tube ($y = 0.025$ m, $x \in [0\text{ m}, 0.05\text{ m}]$), shows the profile for gas temperature at 60 μs superposed over the viscous one-dimensional results, and the analytical inviscid one-dimensional solution. For the two-dimensional problem, the leading edge of the shock becomes slightly more diffuse, and the temperatures in the domain through which the waves have passed are not constant. It is evident that both the one- and two-dimensional cases agree well with the analytical solution.

4.2. Piston

For the two-dimensional piston, the problem is solved after the appropriate non-Galilean transformation (Cochran, 2007) with $\mathscr{F} \neq 0$ and non-ideal state equations. Fig. 4 shows a shaded contour plot of solid volume fraction and solid pressure. The speed of the wavefront at centerline $y = 0.025$ m, $x \in [0\text{ m}, 0.05\text{ m}]$, is nearly identical to that of the one-dimensional piston. However, boundary layer effects are beginning to become evident, particularly in the solid pressure, as evidenced by the slight curvature of the pressure wave

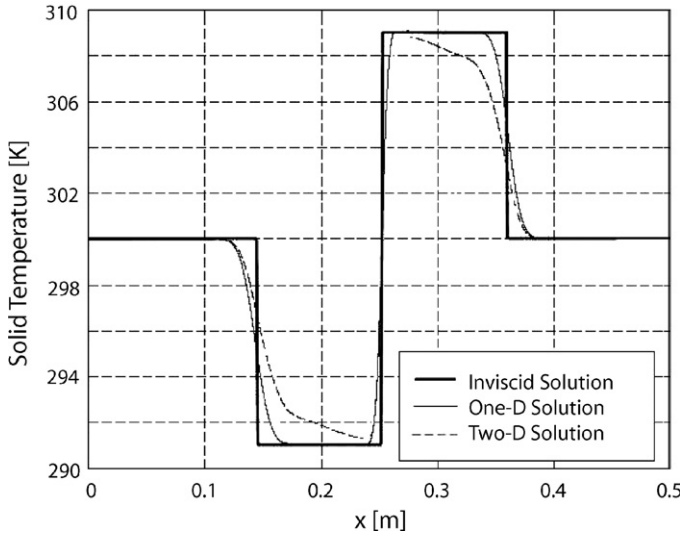

Fig. 3. Comparison of gas temperature profiles through the centerline of the domain for no-slip and periodic boundary conditions in a two-dimensional shock tube at $t = 60$ μs.

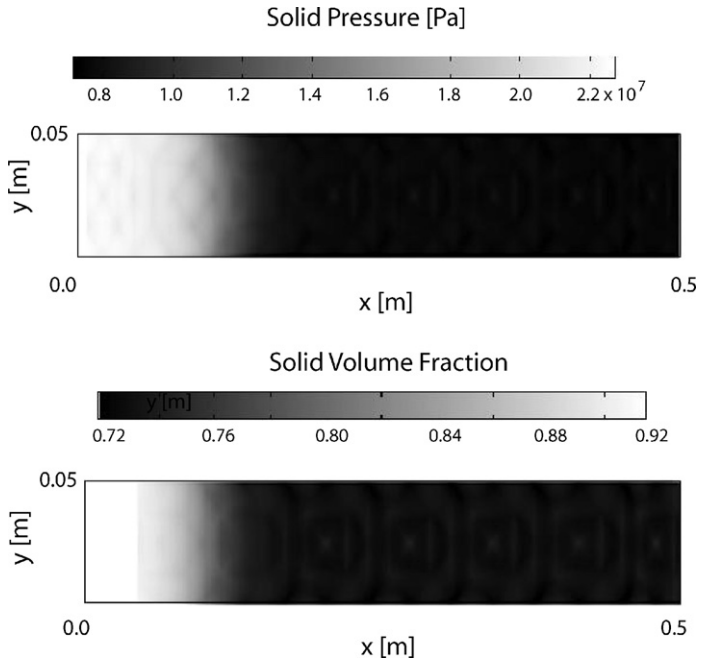

Fig. 4. Solid pressure and volume fraction at $t = 600$ μs for a two-dimensional piston traveling at 100 m/s.

front. The faint diamond patterns in Fig. 4 are likely acoustic waves reflecting in the domain. There are approximately 35–40 grids in the y direction, meaning that the characteristic grid size is $\Delta y \sim 1.25 \times 10^{-3}$ m. Moreover, there are roughly 7–10 grids in the boundary layer region.

5. Discussion

We have shown preliminary results to predict two-dimensional compaction waves with a common, robust multi-dimensional unsteady finite element algorithm. The algorithm produces results which are consistent with

earlier one-dimensional results. Use of this standard algorithm is enabled by the employment of an underlying mathematical model which is guaranteed to be well-posed, satisfies Galilean frame invariance and an entropy inequality, and easily captures shocks via a physical diffusion mechanism. This thus avoids many well-known problems that have long afflicted models of this class. Future work which more fully explores important multi-dimensional questions of stability and wave diffraction are thus possible and should be undertaken.

References

Abgrall, R., Saurel, R., 2003. Discrete equations for physical and numerical compressible mixtures. Journal of Computational Physics 186, 361–396.

Baer, M.R., 1986. Numerical studies of dynamic compaction of inert and energetic granular materials. Journal of Applied Mechanics 55, 36.

Baer, M.R., Nunziato, J.W., 1986. A two-phase mixture theory for the deflagration-to-detonation transition (DDT) in reactive granular materials. International Journal of Multiphase Flow 12, 861–886.

Bdzil, J.B., Menikoff, R., Son, S.F., Kapila, A.K., Stewart, D.S., 1999. Two-phase modeling of deflagration-to-detonation transition in granular material: A critical examination of modeling issues. Physics of Fluids 11, 378–402.

Cochran, M.T., 2007. Two-dimensional viscous compaction in compressible granular materials. MS Thesis, University of Notre Dame.

COMSOL, 2003. FEMBLAB, User's Guide and Introduction.

Gonthier, K.A., 2004. Predictions for weak mechanical ignition of strain hardened granular explosive. Journal of Applied Physics 95, 3482–3494.

Gonthier, K.A., Powers, J.M., 2000. A high resolution numerical method for a two-phase model of deflagration-to-detonation transition. Journal of Computational Physics 163, 376–433.

Kapila, A.K., Menikoff, R., Bdzil, J.B., Son, S.F., Stewart, D.S., 2001. Two-phase modeling of deflagration-to-detonation transition in granular material: reduced equations. Physics of Fluids 13, 3002–3024.

Lowe, C.A., Greenaway, M.W., 2005. Compaction processes in granular beds composed of different particle sizes. Journal of Applied Physics 98, 547.

Lowe, C.A., Longbottom, A.W., 2006. Effect of particle distribution on the compaction behavior of granular beds. Physics of Fluids 18, 066101.

Papalexandris, M.V., 2005. A two-phase model for compressible granular flows based on the theory of irreversible processes. Journal of Fluid Mechanics 517, 103–112.

Powers, J.M., 2004. Two-phase viscous modeling of compaction of granular materials. Physics of Fluids 16, 2975–2990.

Powers, J.M., 2006. Review of multiscale modeling of detonation. Journal of Propulsion and Power 22, 1217–1229.

Powers, J.M., Stewart, D.S., Krier, H., 1989. Analysis of steady copaction waves in porous materials. Journal of Applied Mechanics 56, 15.

Powers, J.M., Stewart, D.S., Krier, H., 1990. Theory of two-phase detonation-part I: modeling. Combustion and Flame 80, 264.

Sandusky, H.W., Bernecker, R.R., 1985. Compressive reaction in porous beds of energetic materials. Naval Surface Weapons Center Eighth Detonation Symposium.

Sandusky, H.W., Liddiard, T.P., 1985. Dynamic compaction of porous beds. Naval Surface Weapons Center Report, 83–256.

Schewendeman, D.W., Wahle, C.W., Kapila, A.K., 2006. The Reimann problem and a high-resolution Godunov method for a model of compressible two-phase flow. Journal of Computational Physics 212, 490–526.

Tiselj, I., Petelin, S., 1997. Modelling of two-phase flow with second-order scheme. Journal of Computational Physics 136, 503–521.

Vreman, A.W., 2007. Macroscopic theory of multicomponent flows: Irreversibility and well-posed equations. Physica D: Nonlinear Phenomena 225, 94–111.